

Article

Improvement of $\text{Co}_3\text{V}_2\text{O}_8$ Nanowire Driven by Morphology for Supercapacitor and Water Splitting Applications

Manesh Ashok Yewale  and Dong Kil Shin *

School of Mechanical Engineering, Yeungnam University, Gyeongsan 38541, Republic of Korea; maneshphd@gmail.com

* Correspondence: dkshin@yu.ac.kr

Abstract: Supercapacitors have a better power density than batteries; however, there is room for improvement in energy density. $\text{Co}_3\text{V}_2\text{O}_8$ nanoparticles were synthesized using the hydrothermal approach, with the reaction duration tuned to enhance energy density. At a 10 h hydrothermal reaction time, bundles of nanowires with void spaces were obtained, demonstrating excellent areal capacitance of 4.67 F/cm^2 , energy density of $94 \mu\text{Wh/cm}^2$, and power density of $573 \mu\text{W/cm}^2$ at a current density of 3 mA/cm^2 . With activated carbon (AC) and $\text{Co}_3\text{V}_2\text{O}_8$ nanoparticles prepared over a 10-h hydrothermal reaction period, an asymmetric supercapacitor (ASC) was assembled. The device performed admirably in terms of energy storage capacity, with an areal capacitance of 781 mF/cm^2 and a volumetric capacitance of 1.43 F/cm^3 . The ASC's cyclic stability demonstrated capacity retention of 83.40% after 5000 cycles. The powering of red LEDs was used to show practical applications. In a 2M KOH electrolyte, the optimized $\text{Co}_3\text{V}_2\text{O}_8$ electrode demonstrated good electrocatalytic performance for the hydrogen evolution process, with an overpotential of 259 mV at a current density of 10 mA/cm^2 . Overall, water splitting studies revealed a potential of 1.78 V with little potential enhancement after 8 h of Chrono potentiometric stability. As a result, $\text{Co}_3\text{V}_2\text{O}_8$ nanoparticles prepared at a 10 h hydrothermal reaction time offer excellent electrode materials for energy storage in supercapacitors and electrocatalytic applications for total water splitting.



Academic Editors: Xianzhong Sun, Xiong Zhang and Changzhou Yuan

Received: 31 December 2024

Revised: 7 March 2025

Accepted: 19 March 2025

Published: 21 March 2025

Citation: Yewale, M.A.; Shin, D.K. Improvement of $\text{Co}_3\text{V}_2\text{O}_8$ Nanowire Driven by Morphology for Supercapacitor and Water Splitting Applications. *Batteries* **2025**, *11*, 118. <https://doi.org/10.3390/batteries11040118>

Copyright: © 2025 by the authors. Licensee MDPI, Basel, Switzerland. This article is an open access article distributed under the terms and conditions of the Creative Commons Attribution (CC BY) license (<https://creativecommons.org/licenses/by/4.0/>).

1. Introduction

Electronic gadgets, rapidly increasing in usage nowadays, operate on energy storage devices. Supercapacitors have emerged as an excellent choice for energy storage in advanced electronic equipment due to their outstanding characteristics such as fast charging time, high energy and power density, light weight, and longevity [1–6]. Their popularity is growing day by day. Nowadays, supercapacitors are used in various electronic devices including portable electronics, sensing devices, and hybrid electric vehicles [7–10]. Supercapacitors are classified into two subclasses based on their energy storage mechanism: electric double-layered capacitors (EDLCs) and pseudocapacitors (PCs). Pseudocapacitors store charge through Faradic reactions on the electrode material's surface, whereas EDLCs store charge through the adsorption of ions on the electrode material's surface. Materials with a high surface area typically exhibit excellent EDLC characteristics. Mostly, carbon-based materials such as graphene oxide [11–13] and carbon nanotubes [14], as well as some metal oxides [15], demonstrate EDLC properties [16]. On the other hand, conducting

polymers [17], transition metal oxides, and metal chalcogenides exhibit charge storage mechanisms typical of pseudocapacitors. Pseudocapacitors have gained popularity as electrochemical energy storage devices due to their large theoretical capacitance, different valences, and diverse electronic architectures. Because of their superior theoretical capacitance, numerous oxidation states, synergistic effects, cost-effectiveness, abundance, and huge potential window, bimetallic metal oxides are now being researched for electrochemical energy storage applications. There have been several study papers on bimetallic oxides such as NiCo_2O_4 [18–20], CuCo_2O_4 [21–23], $\text{Ni}_3\text{V}_2\text{O}_8$ [24,25], and $\text{Co}_3\text{V}_2\text{O}_8$ [26,27]. Bimetallic oxides have a higher energy storage capacity than monometal oxides such as NiO [28,29], Co_3O_4 [23,30], and V_2O_5 [31] due to their synergistic effect and numerous oxidation states. Researchers are particularly interested in $\text{Co}_3\text{V}_2\text{O}_8$. Cobalt-based bimetallic oxides have gained significant interest because of their inherent properties such as strong electrical conductivity, simple synthesis procedures, and great electrical stability [32,33]. Cobalt also has a large theoretical capacitance and a great reversible redox ability and corrosion resistance [34]. The majority of cobalt-based metal oxides have a densely packed cubic spinel structure [35]. Recently, the hydrogen evolution reaction (HER) via electrocatalysis and supercapacitors has piqued the interest of many researchers in the field of environmentally benign and highly effective electrode materials for energy storage and conversion. Metal oxides with bifunctional applications are receiving more attention for economic reasons [36]. Noble metals with high electrocatalytic activity include palladium and platinum. However, their widespread adoption is hampered by high costs. As a result, it is critical to develop electrode materials that are cost-effective, high-efficiency, and environmentally benign for electrocatalytic and supercapacitor applications [37–40]. Porous microwires have potential uses in electrocatalysis and supercapacitor technology. For multifunctional applications, several cobalt–vanadium oxide microstructures have been described. H. Wang et al. reported on the hydrothermal synthesis of hexagonal nanosheets of $\text{Co}_2\text{V}_2\text{O}_7$ for hybrid supercapacitor applications. They have a high energy storage capacity [41]. H. Sun, on the other hand, developed 3D microflowers with exceptional cycle stability for asymmetric supercapacitor electrodes. These were produced using a chemical technique at precise temperatures and precursor molar concentrations. At 1 A/g, the electrode demonstrated a remarkable energy storage capacity of 351 F/g. The energy storage capacity of an asymmetric supercapacitor (ASC) developed with the optimized electrode and reduced graphene oxide (rGO) was 19 Wh/kg. It had a power density of 375.8 W/kg, having a potential range of 0–1.5 V [42]. G. P. Sharma employed hydrothermal synthesis for synthesizing $\text{Co}_3\text{V}_2\text{O}_8$ and S- $\text{Co}_3\text{V}_2\text{O}_8$ nanosheets for supercapacitor applications. The $\text{Co}_3\text{V}_2\text{O}_8$ nanosheets demonstrated a remarkable storage capacity of 337.8 mAh/g at 2 A/g [43]. There have been few reports on the use of cobalt-mixed metal oxide for catalysis. G. M. Thorat reported on octahedral cobalt vanadate synthesized for an oxygen evolution reaction (OER) employing a deep eutectic solvent method [44]. D. K. Singh addressed cobalt-based vanadium mixed oxide nanocrystals coupled with polymer electrodes for electrochemical water oxidation, demonstrating their electrocatalysis applications [45]. J. Han also reported on cobalt vanadium spinel synthesized at various Co/V molar ratios utilizing the hydrothermal process for electrocatalysis applications [46]. The usage of cobalt-based mixed vanadium oxide as a supercapacitor and electrocatalysis electrode has received little attention.

When synthesizing $\text{Co}_3\text{V}_2\text{O}_8$ (CVO) nanowires, the influence of the hydrothermal reaction duration was investigated in order to achieve a homogeneous nanowire with a porous structure. While other parameters remained constant, the hydrothermal reaction time was increased from 4 h to 16 h. The reaction time has an effect on the surface microstructure of $\text{Co}_3\text{V}_2\text{O}_8$. Nanowire bunch production began at lower hydrothermal

reaction durations, and the development of these nanowires accelerated as the reaction time increased. Initial little bundles of nanowires began to develop after a hydrothermal reaction period of 10 h. These clusters merged at one end, leaving empty space at the other. This open area is beneficial for ion diffusion, increasing the electrode's capacity. The 10 h hydrothermal reaction time electrode displayed exceptional areal energy storage capacity and electrocatalytic activity for water splitting via HER and OER. The optimized electrode and activated carbon (AC) were used to make an asymmetric supercapacitor. The ASC demonstrated exceptional areal energy storage capacity and power density. A two-electrode device was constructed for practical applications, and it demonstrated its higher energy storage capability by lighting red LEDs. The $\text{Co}_3\text{V}_2\text{O}_8$ electrode formed by a 10 h hydrothermal reaction appears to be an acceptable electrode material for supercapacitor and electrolysis applications based on the findings obtained for the $\text{Co}_3\text{V}_2\text{O}_8$ nanowires.

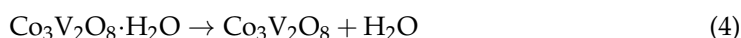
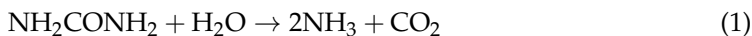
2. Experimental

2.1. Chemicals

All chemicals, particularly cobalt nitrate hexahydrate ($\text{Co}(\text{NO}_3)_2 \cdot 6\text{H}_2\text{O}$) (98%), urea ($\text{CO}(\text{NH}_2)_2$) (99%), ammonium metavanadate (NH_4VO_3) (99%), acetone (CH_3CO) (99%), ethanol ($\text{C}_2\text{H}_6\text{O}$) (99.5%), polyvinylidene fluoride (PVDF), N-Methyl-2-pyrrolidone (NMP), and potassium hydroxide (KOH) (85%), were sourced from Sigma-Aldrich (St. Louis, MO, USA) and used without extra purification processing. HCl were provided by Daejung Chemical (Siheung-si, Republic of Korea).

2.2. Preparation of $\text{Co}_3\text{V}_2\text{O}_8$ (CVO) Nanowires

A simple hydrothermal process was used to prepare $\text{Co}_3\text{V}_2\text{O}_8$ nanowires. To begin the synthesis, 40 mL of water was mixed with 4.8 mL of cobalt nitrate, 7.2 mL of ammonium metavanadate, and 2.24 mL of urea to form a homogenous solution. After stirring, the entire solution was transferred and carefully sealed into a 100 mL Teflon liner reactor. The hydrothermal reactor was then placed in a fan-forced furnace for 4 h to maintain a temperature of 140 °C. After the reaction was completed, the reactor was allowed to cool naturally to ambient temperature. After cooling, the produced product was filtered through filter paper and the residue was washed with water and ethanol several times. The washed $\text{Co}_3\text{V}_2\text{O}_8$ powder was dried overnight at 60 °C. Following the drying procedure, the $\text{Co}_3\text{V}_2\text{O}_8$ powder was annealed at 400 °C for 4 h. After drying, the $\text{Co}_3\text{V}_2\text{O}_8$ powder was given the designation CVO_U_4h. The reaction mechanism for the formation of $\text{Co}_3\text{V}_2\text{O}_8$ nanowires is represented by reactions (1)–(4) [47]. A similar approach was used for the synthesis of $\text{Co}_3\text{V}_2\text{O}_8$ powder at 7 h, 10 h, and 16 h of hydrothermal reaction time, and the products were called CVO_U_7h, CVO_U_10h, and CVO_U_16h, respectively. $\text{Co}_3\text{V}_2\text{O}_8$ nanowires prepared for different hydrothermal reaction times were utilized for further characterization and study with similar nomenclature.



2.3. Characterizations

X-ray diffraction (XRD; PANalytical, Almelo, The Netherlands) with CuK radiation was used to analyze the crystal structure and phase evolution of the microparticles. The surface morphology and elemental mapping of the nanoparticles were studied using field-

emission scanning electron microscopy (FE-SEM; S-4800 HITACHI, Ltd., Tokyo, Japan). X-ray photoelectron spectroscopy (XPS; K-alpha, Thermo Scientific, Altrincham, UK) was used to analyze the chemical composition of the surface. To investigate element mapping and surface morphology further, high-resolution transmission electron microscopy (HRTEM; Tecnai F21, FEI Company, Hillsboro, OR, USA) was used. On a ZIVE SP5 (WonAttech, Seoul, South Korea) electrochemical workstation, electrochemical tests such as cyclic voltammetry (CV), electrochemical impedance spectroscopy (EIS), galvanostatic charge–discharge (GCD), linear sweep voltammetry (LSV), and cyclic stability measurements were performed. These measurements were performed using a three-electrode configuration consisting of a platinum counter electrode, the active material as a working electrode, and an Ag/AgCl reference electrode.

2.4. Electrode Preparation

The working electrode was made with extreme accuracy and attention to allow for a complete examination of the electrochemical performance of the active substance. Using an NMP solution, a slurry of the active material ($\text{Co}_3\text{V}_2\text{O}_8$), PVDF, and carbon black (CB) in an 80:10:10 ratio was made and employed to form the electrode. To achieve a clean electrode surface, the $1 \times 2 \text{ cm}^2$ Ni-foam region was extensively cleaned with hydrochloric acid to remove any contaminants. The dried Ni-foam substrate was then utilized to prepare the final electrode. Prior to electrochemical investigation, the active material slurry was drop-cast onto the Ni substrate's $1 \times 1 \text{ cm}^2$ active region and dried overnight at 60°C . An identical procedure was used for preparing the working electrode and activated carbon electrode. Only activated carbon (AC) was used instead of $\text{Co}_3\text{V}_2\text{O}_8$ nanoparticles in the fabrication of the activated carbon (AC) electrode.

2.5. Electrochemical Measurement

The active electrode ($\text{Co}_3\text{V}_2\text{O}_8$) served as the working electrode in the three-electrode arrangement, platinum served as the counter electrode, and an Ag/AgCl electrode served as the reference electrode. The ZIVE-SP5 WonAttech workstation was used to conduct electrochemical tests with a 2M KOH electrolyte. A two-electrode design was prepared for the practical application. The $\text{Co}_3\text{V}_2\text{O}_8$ nanoparticles were synthesized after a 10-h hydrothermal process that was utilized to prepare two electrode configurations. For 20 min, both the CVO_U_10h electrode and the AC electrode were soaked in 2M KOH. Following that, the two electrodes were securely wrapped in paraffin paper, with wetted filter paper put between them. Using a workstation, the device was used to investigate cyclic voltammetry (CV), galvanostatic charge–discharge (GCD), electrochemical impedance spectroscopy (EIS), and electrode stability.

3. Result and Discussion

3.1. Physicochemical Properties of the $\text{Co}_3\text{V}_2\text{O}_8$ Nanoparticles

To investigate the phase evolution and crystalline structure of CVO nanowires, powder X-ray diffraction was used. Figure 1 depicts the XRD diffraction pattern of CVO nanowires generated by different hydrothermal reaction time frames ranging from 4 h to 16 h. Reflections were seen in the XRD spectra of all nanoparticles at 2θ angles of 21.15° , 27.42° , 31.37° , 32.99° , 35.82° , 36.81° , 48.35° , 48.84° , 57.41° , and 63.84° . These are clearly matched with the JCPDS database of 01-074-1487, which has an orthorhombic phase with lattice parameters of $a = 8.30 \text{ \AA}$, $b = 11.50 \text{ \AA}$, and $c = 6.03 \text{ \AA}$ and 2θ angles of 22.47° , 23.98° , 39.74° , and 50.44° match with the JCPDS database of 00-022-0599, confirming the nanoparticles' mixed $\text{Co}_3\text{V}_2\text{O}_8$ phase growth. The peak intensity of the 211 plane grows as the hydrothermal

reaction time increases, and the XRD findings agree with those of Avi et al. [10], Mushtaq et al. [48], and Samuel et al. [49].

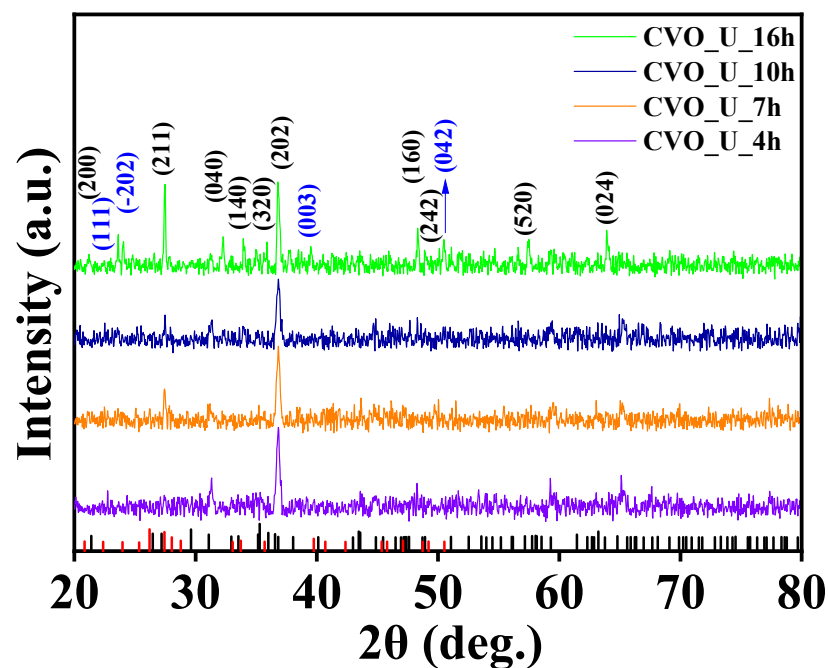


Figure 1. XRD spectra of $\text{Co}_3\text{V}_2\text{O}_8$ nanoparticles at 4 h, 7 h, 10 h, and 16 h of hydrothermal reaction time.

The elemental state, purity, and chemical composition of the prepared CVO_U_10h electrode were investigated through X-ray photoelectron spectroscopy (XPS). Figure 2a shows the survey scan spectra of the CVO_U_10h electrode over the range of 0–1200 eV, showing the presence of sharp peaks at 516.4 eV, 780.19 eV, and 529.93 eV and confirm the existence of vanadium (V2p), cobalt (Co2p), and oxygen (O1s) in the CVO_U_10h electrode. The elemental compositions of the XPS results were well matched with the EDX results, which confirm the formation of $\text{Co}_3\text{V}_2\text{O}_8$ stoichiometrically. Figure 2b shows the spin orbit narrowing two core-level spectra of Co 2p_{3/2} and Co 2p_{1/2}. Co 2p_{3/2} and Co 2p_{1/2} were observed at binding energies of 780.01 eV and 795.81 eV, with a separation of 15.8 eV. The Co 2p_{3/2} and Co 2p_{1/2} spectra were split into two peaks, showing the presence of Co^{2+} and Co^{3+} . The peaks appearing at 779.81 eV and 794.81 eV show the presence of Co^{3+} , and the peaks observed at 781.23 eV and 796.60 eV show the presence of Co^{2+} in the CVO_U_10h electrode. Additionally, two shakeup satellite peaks were observed at 786.92 eV and 803.52 eV, which is in good agreement with the results [43]. The XPS study reveals the presence of Co ions with a Co^{2+} oxidation state [50,51].

The O 1s spectra of the CVO_U_10h electrode are shown in Figure 2c. Three peaks at binding energies of 529.87 eV (O_1), 530.18 eV (O_{II}), and 531.87 eV (O_{III}) are attributed to the O 1s spectra. The peak at 531.87 eV (O_{III}) can be ascribed to oxygen defects. The peak at 530.18 eV (O_{II}) is attributed to chemo-absorbed and physio-absorbed water molecules, and further peaks corresponding to the binding energy of 529.87 eV (O_1) are attributed to the metal–oxygen bond (Co–O and V–O) [43]. The deconvolution spectra of the V are shown in Figure 2d, attributed to the two peaks of V 2p_{3/2} and V 2p_{1/2} at binding energies of 516.41 eV and 524.11 eV. The peaks corresponding to 516.34 and 523.54 confirm the existence of the V^{+4} oxidation state, and the peaks attributed to 517.18 and 524.49 correspond to the V^{+5} oxidation state [50]. Overall, the XPS study confirmed the existence, chemical composition, and purity of Co, V, and O in the CVO_U_10h sample. All CVO_U_10h nanowire surface microstructures were examined using field emission scanning electron microscopy

(FESEM) and transmission electron microscopy (TEM). At various magnifications, Figure S1 depicts an FESEM micrograph of the CVO nanowires prepared over various hydrothermal reaction periods ranging from 4 h to 16 h. Figure S1(a1–a4) shows FESEM micrographs of CVO_U_4h nanowires obtained after 4 h of hydrothermal reaction time. Because of the formation of nanowires, these micrographs have spherical forms. The nanowires grow from the core of the sphere, with one end linked to the center and the other end free, like flower petals. Each nanowire is independent at the free end, which provides a better environment for electrolyte ion insertion and extraction during the electrochemical supercapacitor charging and discharging process. As the hydrothermal reaction period extends from 4 h to 7 h, some of the nanowires begin to cluster together and join together, as seen in Figure S1(b1–b4). Furthermore, additional CVO nanowires begin to form, influencing the electrode's cyclic voltammetry (CV) and galvanostatic charge–discharge (GCD) profiles. The joining of the nanowires forms a network, which improves electrical conductivity and facilitates ion movement throughout the charging and discharging processes. A distinct, uniform spherical shape with a swarm of linked nanowires is found after the 10 h hydrothermal reaction period. Clusters are formed by small bundles of interconnected nanowires (Figure 3a–d), with numerous bundles connected to one another while leaving vacant spaces between them, as shown in Figure S1(c1–c4). These void regions are advantageous for simple electrolyte ion entrance with few impediments, and their impacts may be seen in the electrochemical performance of the CVO_U_10h electrode. It has a wider area under the CV profile curve and takes longer to charge and discharge. The 10 h hydrothermal reaction time appears to be an important optimized parameter for achieving the desired microstructure of the CVO nanowires. Figure S1(d1–d4) shows an FESEM micrograph for 16 h of hydrothermal reaction, in which the surface microstructure is completely clumped together due to the increased thickness of the nanowires and reduced vacant space between the bundles. As shown in the CV and GCD profiles, the reduction in empty area results in a reduction in energy storage capacity. The schematic shown in Figure 4 depicts the growth mechanism of $\text{Co}_3\text{V}_2\text{O}_8$ nanoparticles during a 10 h hydrothermal reaction based on structural and surface microstructural investigations. Cobalt vanadium nanowires are prepared at the appropriate hydrothermal reaction time of 10 h, and their continued development leads to the formation of nanowire frameworks. Energy-dispersive X-ray spectroscopy (EDS) measurements were used to determine the elemental composition of all CVO nanowires. The EDS spectra of CVO_U_10h nanoparticles prepared at 10 h of hydrothermal reaction time are depicted in Figure 3e, and comparative EDS spectra for all nanoparticles are shown in Figure S2a–d. Sharp EDS peaks indicate the presence of cobalt, vanadium, and oxygen. The X-ray diffraction (XRD) and EDS data show that the intended phase and stoichiometric cobalt vanadium oxide were formed. Figure 3f–h displays the elemental mapping of the CVO_U_10h sample, which demonstrated that the Co, V, and O distributions in the nanoparticles were uniform. The surface microstructure of CVO_U_10h nanowires was investigated using transmission electron microscopy (TEM) to analyze their morphology, structural arrangement, and potential effects on electrochemical performance. Figure 5 displays TEM micrographs of CVO_U_10h nanoparticles at different magnifications, highlighting their distinct nanostructural characteristics.

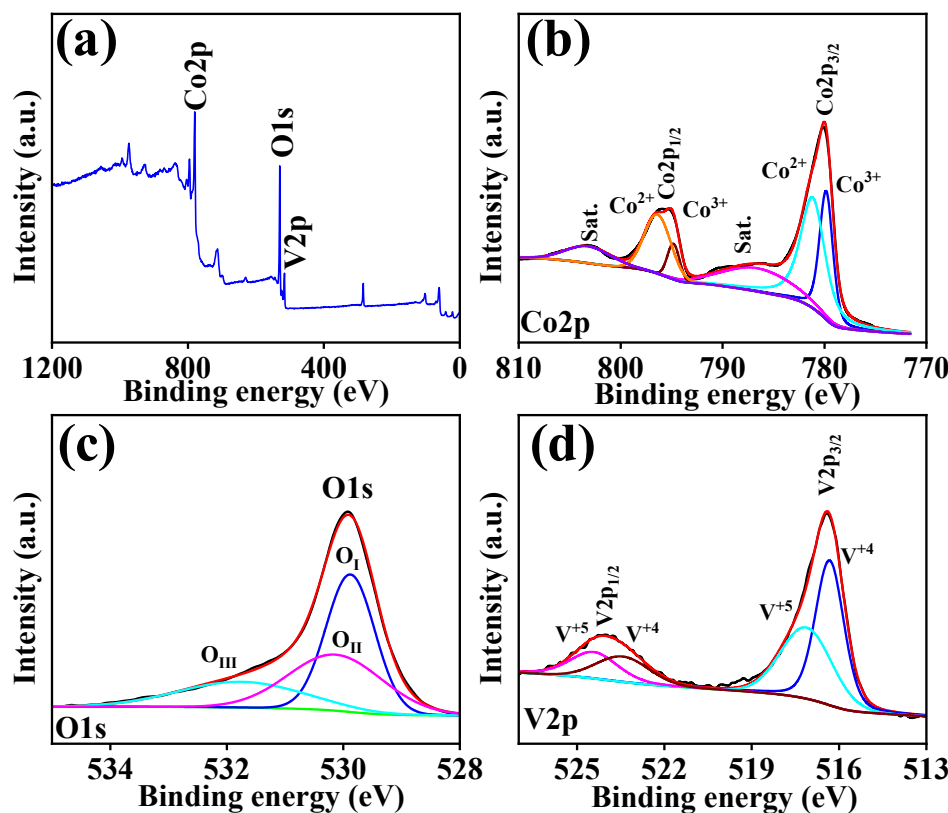


Figure 2. XPS spectra of CVO_U_10h nanoparticles: (a) survey, (b) cobalt, (c) oxygen, and (d) vanadium.

Figure 5a illustrates the formation of nanowires, which are observed to interconnect and assemble into bundles. This bundled configuration significantly enhances the network connectivity of the electrode material, thereby improving charge transport and electron mobility in electrochemical processes. The interconnected nanowire structure offers a continuous conductive pathway for electron flow, significantly enhancing the performance of the supercapacitor, especially regarding power density and cycle stability. The bundling effect preserves the mechanical integrity of the electrode and mitigates excessive degradation across multiple charge–discharge cycles. At higher magnifications (Figure 5b–d), the nanowires demonstrate minor splitting at their free ends, resulting in the development of voids or pores among the individual nanowires. The inter-nanowire gaps significantly influence the electrochemical behavior of the material by enhancing the available surface area for electrolyte interaction and facilitating rapid ion transport. The existence of these disparity areas facilitates the efficient diffusion of a substantial number of electrolyte ions into the electrode material, thereby significantly improving its charge storage capacity. Figure 5e,f displays high-resolution TEM images that illustrate the crystal plane spacing (d-spacing) of the CVO_U_10h electrode material. Figure 5e clearly displays well-defined crystal planes, indicating a high degree of crystallinity in the synthesized material. Fast Fourier transform (FFT) analysis (Figure 5h) revealed a d-spacing value of 0.315 nm for CVO_U_10h, aligning with the characteristic lattice spacing of $\text{Co}_3\text{V}_2\text{O}_8$. The crystallographic data offers direct evidence of the ordered atomic structure in the nanowires, essential for ensuring stable electrochemical performance during extended cycling. Figure 5g presents the selected area electron diffraction (SAED) pattern of CVO_U_10h nanoparticles. The distinct ring patterns observed in the SAED image confirm the material's polycrystalline nature. The observed diffraction rings align with various crystallographic planes of $\text{Co}_3\text{V}_2\text{O}_8$, demonstrating strong concordance with the X-ray diffraction (XRD) analysis. The correlation between the SAED and XRD results confirms that the synthesized nanoparticles possess a highly

crystalline and polycrystalline structure, conducive to enhanced electrochemical activity. Surface examination of the CVO_U_10h nanowires was investigated using N₂ adsorption/desorption BET studies. Figure S3 depicts the N₂ adsorption/desorption isotherm with a typical Type I-V adsorption and desorption curve. CVO_U_10h nanowires have a surface area of 41.26 m²/g. The inclusion of tiny nanoballs with empty spaces may give an enormous surface area, allowing for improved interaction between the electrode and the electrolyte. Tiny nanoparticles provide a large surface area to enhance the energy storage capacity of the CVO_U_10h electrode when compared to other electrodes.

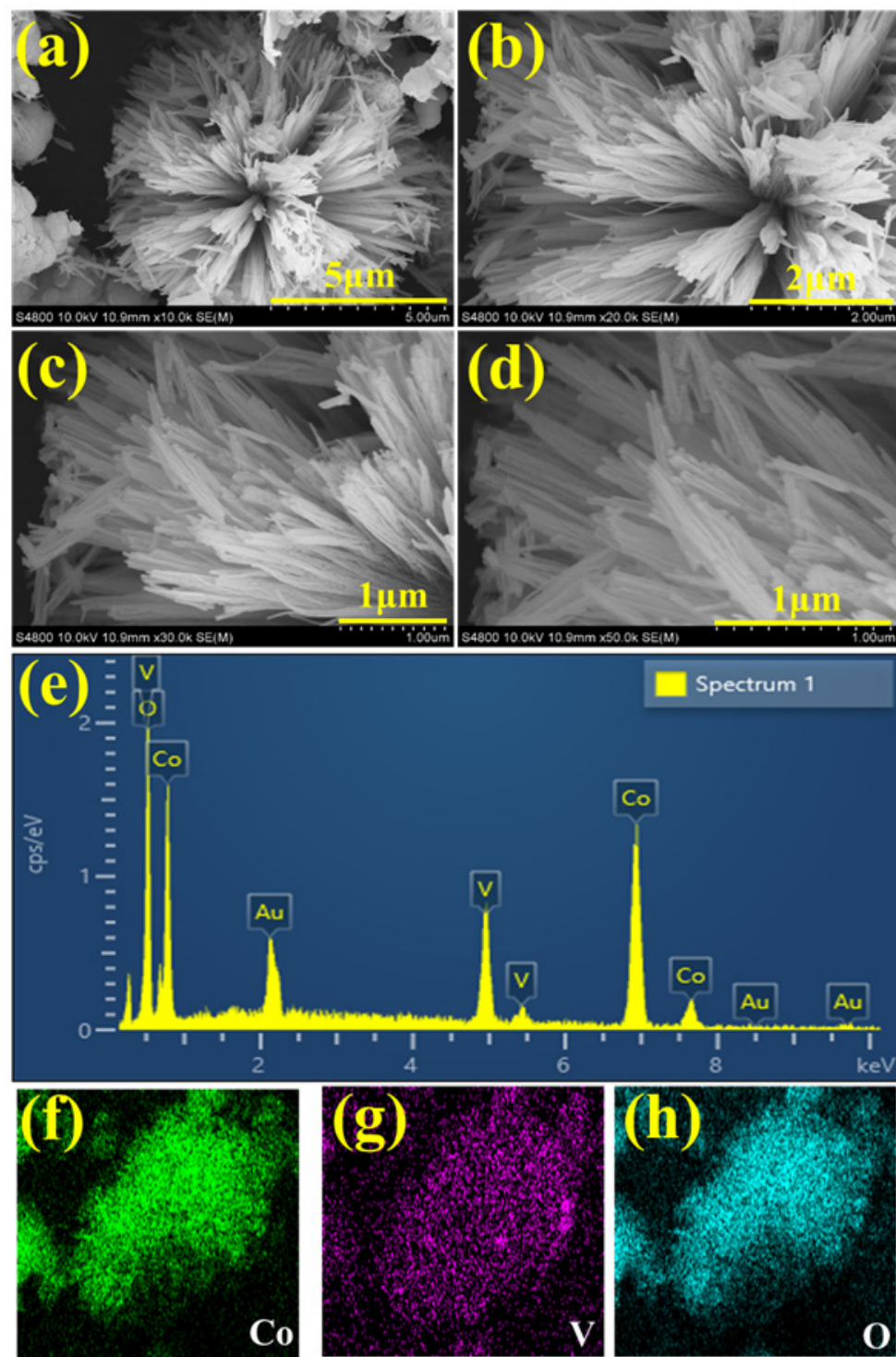


Figure 3. (a–d) FESEM micrographs at different magnifications, (e) EDS spectra, and (f–h) elemental mapping of CVO_U_10h nanowires.

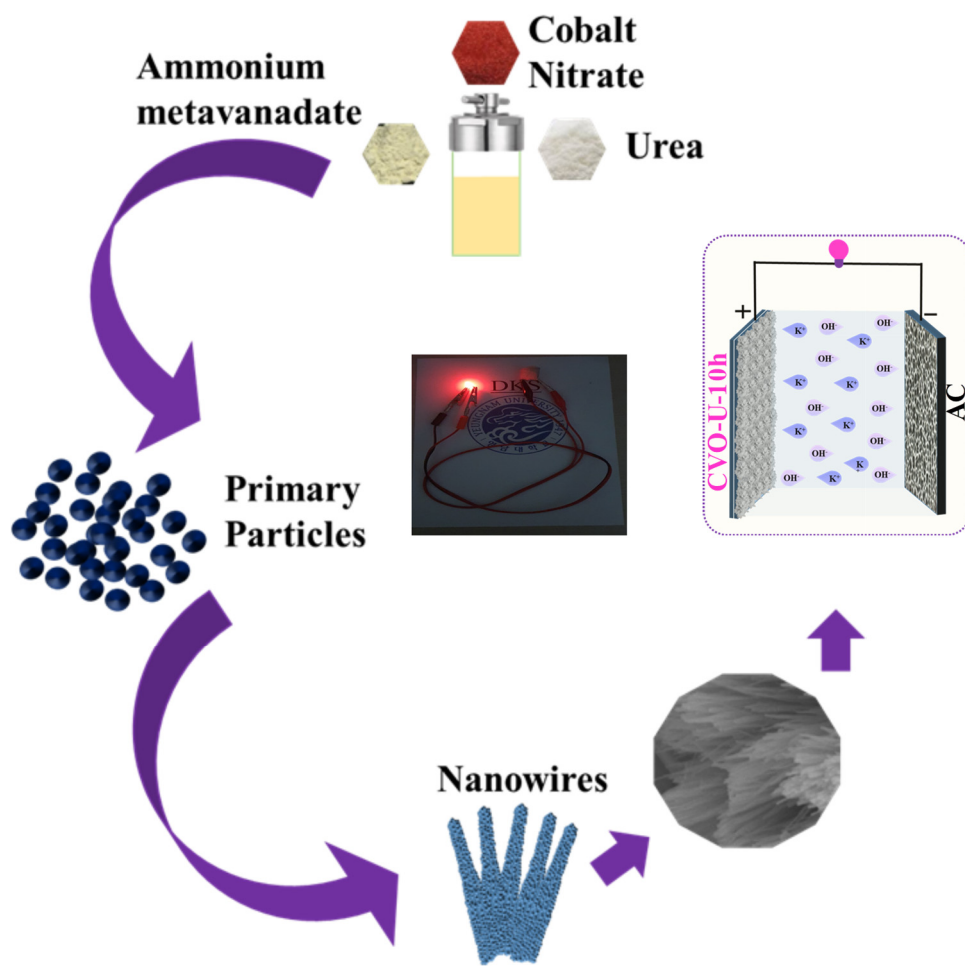


Figure 4. Schematic growth mechanism of $\text{Co}_3\text{V}_2\text{O}_8$ nanoparticles prepared using a hydrothermal approach.

3.2. Electrochemical Performance and Kinetics Analyses of the $\text{Co}_3\text{V}_2\text{O}_8$ Nanoparticles

The electrochemical analysis of all the CVO_U electrodes was carried out in a 2M KOH electrolyte using cyclic voltammetry and galvanostatic charge–discharge measurements. Figure S4 depicts the CV profiles of all CVO_U electrodes. The area under the curve grows with increasing hydrothermal reaction time, as shown in Figure 6a. The electrode's energy storage capacity rises with increasing area. All electrodes show distinct redox peaks, demonstrating charge storage via pseudocapacitive behavior. The redox peaks shift as the scan rate increases, indicating fast and reversible redox kinetics, a characteristic of pseudocapacitive behavior [52]. As shown by the CV profile, the hydrothermal reaction period influences the surface microstructure of CVO_U nanowires. Nanowires grow after 4 h of hydrothermal processing, giving additional active sites for redox reactions. With a 7-h reaction, nanowires link sideways, increasing interaction, as can be seen in the CV profile of the CVO_U_10h electrode, which has an expanded area in the CV profile curve, as shown in Figure S4c. Nanowire bundles with a large active surface area provide a grown conjunction and a large active surface area for a 10-h hydrothermal reaction. Figure 6a depicts the area of the CV profile impacted by the hydrothermal reaction time. When compared to the other electrodes, the area under the curve for the 10-h hydrothermal reaction was larger, indicating superior energy storage capabilities. In a 16-h reaction, however, the nanowire size increases, resulting in a loss in active surface area and storage capacity. The electrode prepared in a 10-h hydrothermal reaction has a void space with connected nanowire CVO nanoparticles which provide a high energy storage capacity, making it

an attractive electrode material for energy storage applications. The CV profiles of all electrodes were employed to examine the kinematics of their electrochemical characteristics in more depth. The charge distribution was calculated using the 'b' value, which reflects two different charge storage processes, namely, capacitive and diffusive processes. In this case, 'b' = 1.0 for the capacitive process and 'b' = 0.5 for the diffusive process. Charge storage via diffusion and capacitive processes is indicated by values of $0.5 < b < 1.0$. The following equations were used to calculate the b values from the CV profiles:

$$i = a \times v^b \quad (5)$$

$$\log(i) = b \cdot \log(v) + \log(a) \quad (6)$$

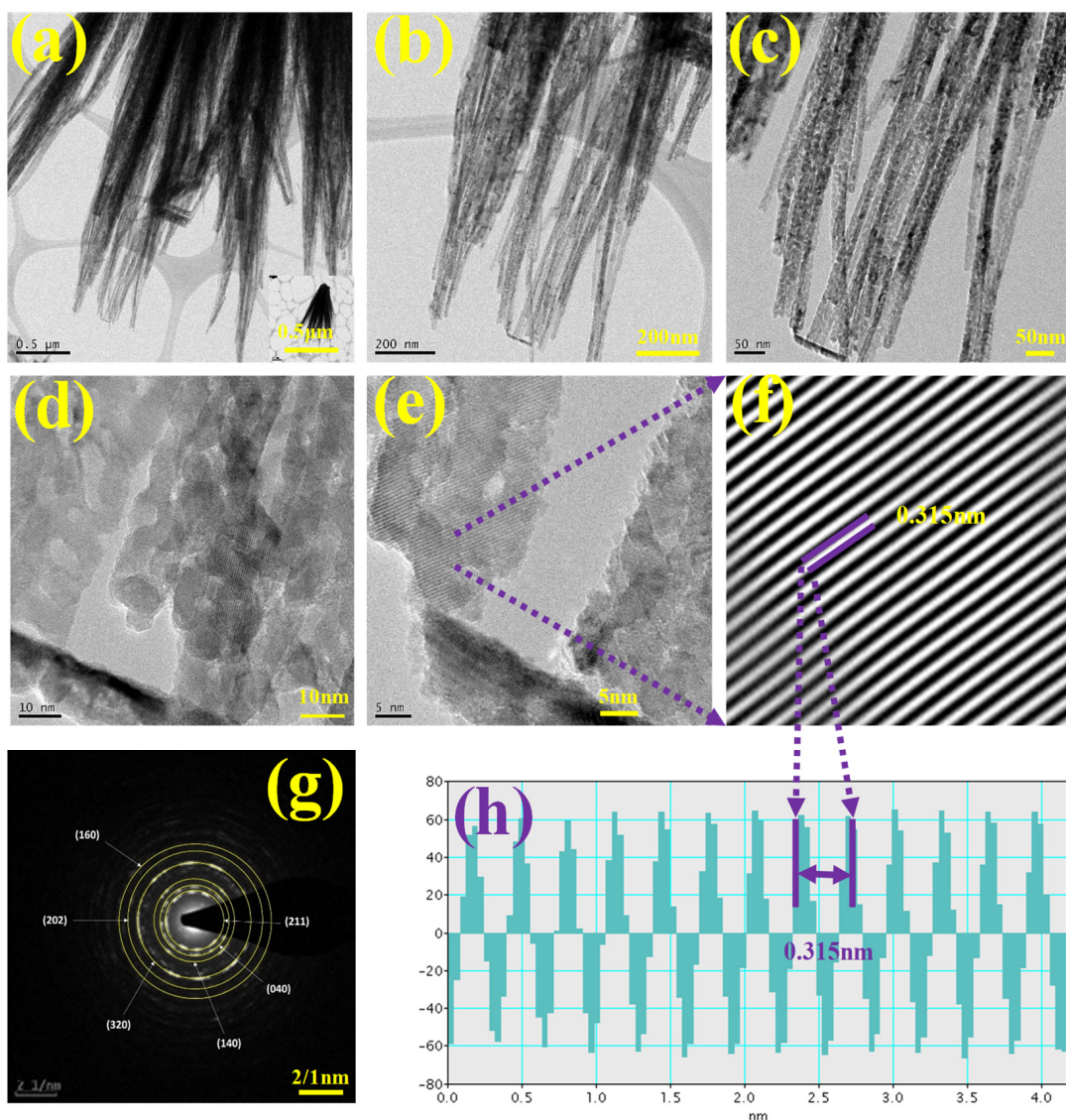


Figure 5. (a–d) TEM at different magnifications, (e,f) d-spacing image, (g) SEAD pattern, (h) FFT pattern for d-spacing CVO_U_10h nanoparticle.

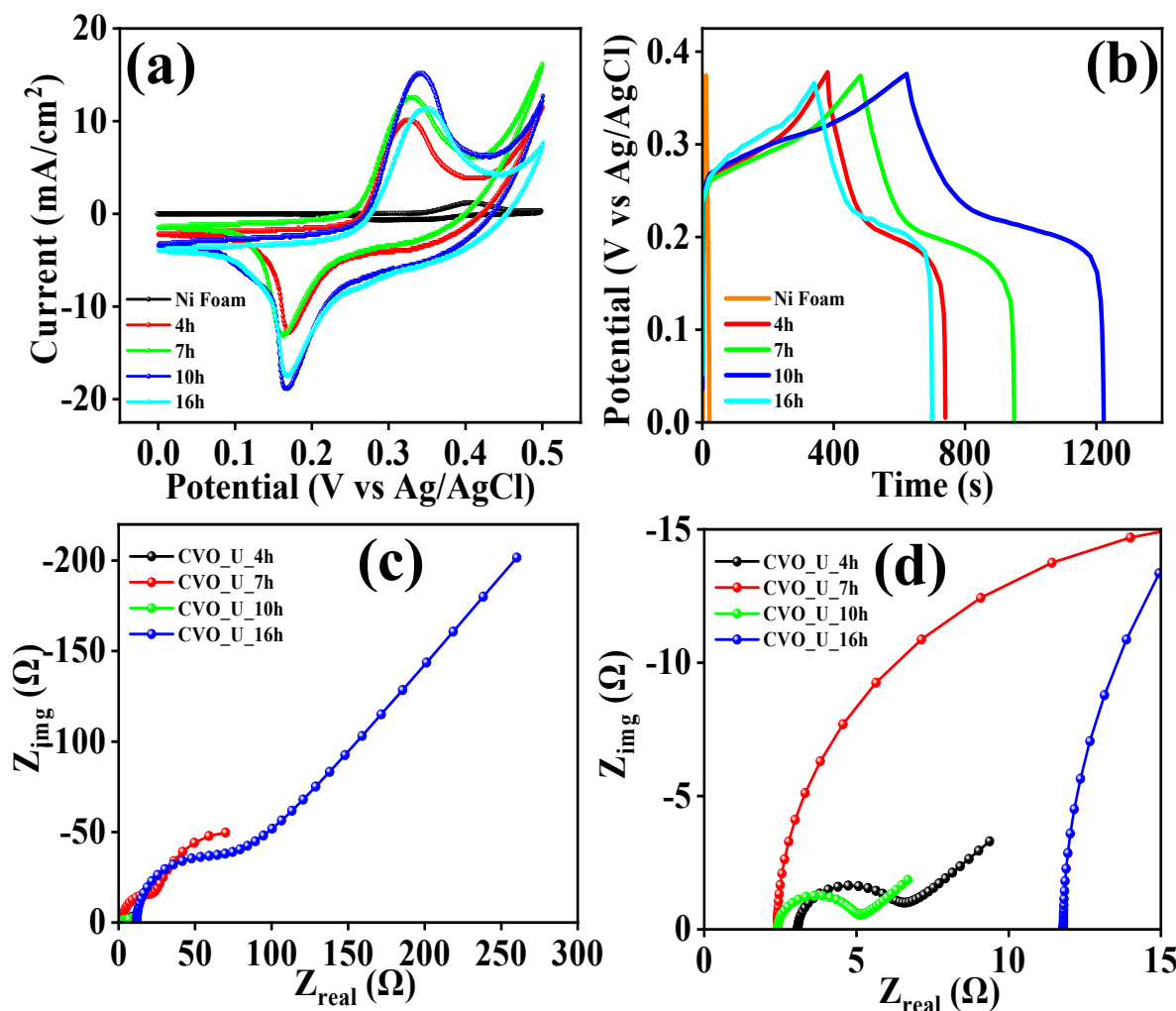


Figure 6. (a) Comparative CV profile, (b) comparative GCD profile, and (c,d) EIS spectra of Co₃V₂O₈ nanowires prepared at different hydrothermal reaction times.

The values were calculated using a log(*i*) vs. log(*v*) plot, as shown in Figure 7a,b, where '*v*' is the scan rate and '*i*' is the peak current corresponding to the scan rate. The 'b' values for the CVO_U_10h electrode are 0.44 and 0.39 for the cathode and anode, suggesting that the diffusion process dominates in the charge process. This might be ascribed to the bundle-like microstructures containing void spaces, which allow electrolyte ions to easily diffuse during the charge and discharge processes [53,54]. The computation of the b value reveals the combined capacitive and diffusion processes. At constant potential, the total current in a CV profile is caused by pseudo capacitance from diffusion-controlled contributions and double-layer capacitance from surface-controlled contributions. These contributions are calculated using the formulae below.

$$i(V) = k_c v + k_d v^{0.5}; \frac{i(V)}{v^{0.5}} = k_c/v^{0.5} + k_d \quad (7)$$

Here, $k_c/v^{0.5}$ denotes capacitive current contributions and k_d denotes diffusion-controlled contributions. The values of k_c and k_d were calculated using Equation (7) with different scan rates. Figure 7c depicts the capacitive and diffusion-controlled current contributions of the CVO_U_10h electrode at a scan rate of 5 mV/s. The 'b' value of the CVO_U_10h electrode shows a larger diffusion contribution at 5 mV/s, implying a larger diffusion contribution, presumably owing to the bundle nanowire with empty space providing a higher diffusion contribution. Figure 7d shows the capacitive and diffusion-

controlled contributions at various scan rates, with the diffusion-controlled contribution decreasing as the scan rate increases [53]. The 'b' values were calculated to demonstrate that the diffusion process outperforms the capacitive process, and the current contribution at constant potential also shows a current owing to the diffusion-controlled contribution. This indicates that the diffusion coefficient for the related electrode may be higher. The diffusion coefficients were computed using the cyclic voltammetry (CV) profile spectra provided in Figure 8a,b and Equation (8). The diffusion coefficient of the CVO_U_10h electrode is higher than that of the other electrode, measuring $4.2 \times 10^{-7} \text{ cm}^2/\text{s}$ for the anodic curve and $4.5 \times 10^{-7} \text{ cm}^2/\text{s}$ for the cathodic curve, respectively. The existence of vacuum spaces between the nanowire bundles may account for the high diffusion coefficient, allowing for effortless insertion and extraction of ions during the electrochemical reaction process. This demonstrates that the diffusion contribution for the CVO_U_10h electrode is higher than the capacitive contribution, and these results are compatible with the 'b' value and current contribution. The diffusion coefficient values are listed in Table 1.

$$i_p = 0.4463 \times A \times F \times C \times \sqrt{\frac{nFDv}{RT}} \quad (8)$$

$$i_p = 0.227 AFCnk^0 \left[-\left(\frac{nF\alpha}{RT} \right) (E_p - E^0) \right] \quad (9)$$

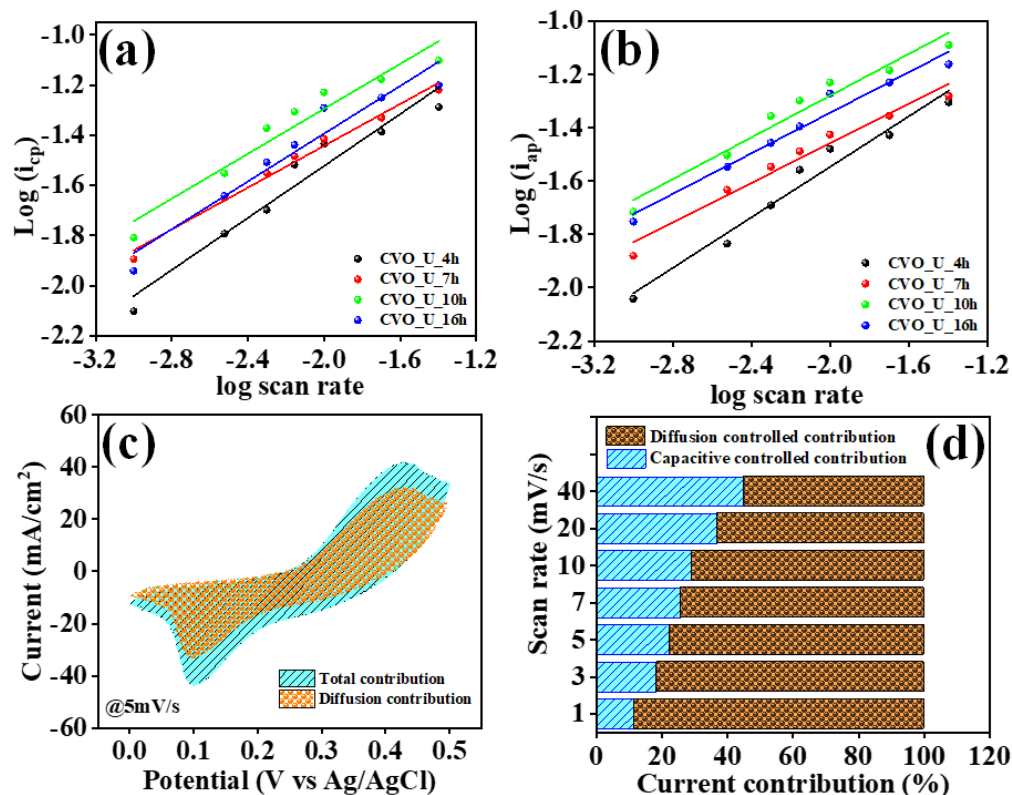


Figure 7. (a,b) $\log(i)$ vs. $\log(v)$ for b values, (c) diffusive and capacitive current contributions at a 5 mV/s scan rate, and (d) diffusive and capacitive current contributions at different scan rates for CVO_U_10h nanoparticles.

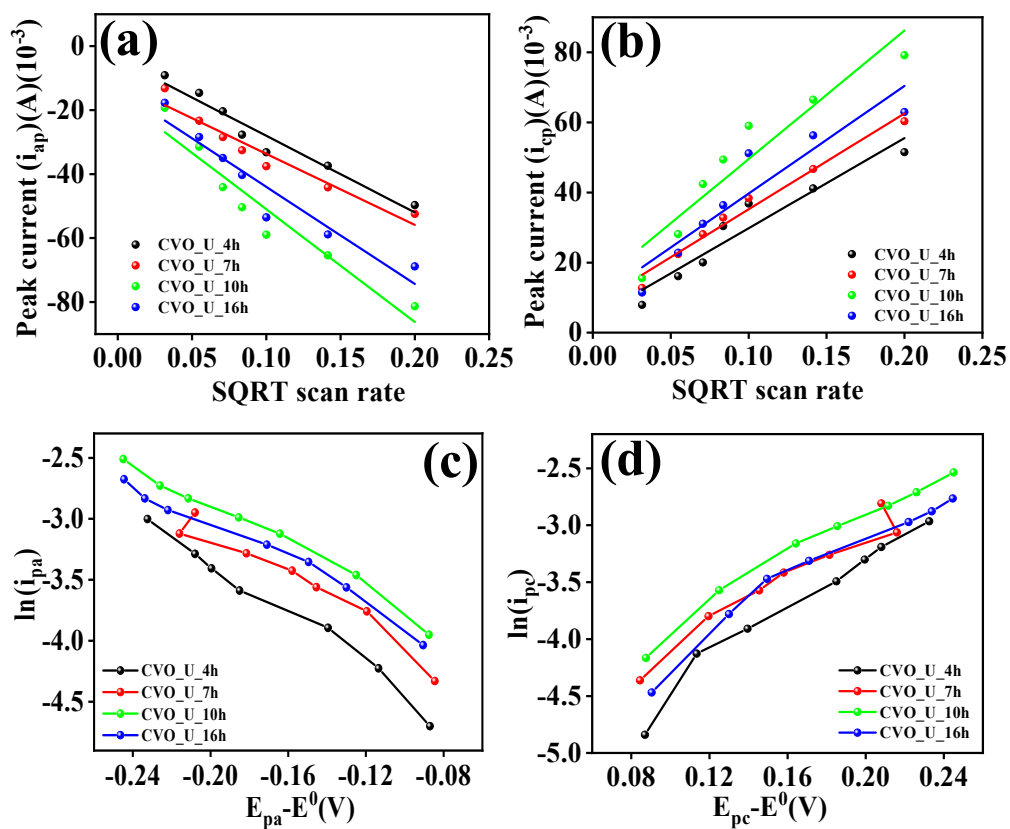


Figure 8. (a,b) Peak current (i_p) vs. SQRT of v for the diffusion coefficient, (c,d) $\ln(i)$ vs. $E_p - E^0$ for the transfer coefficient and standard rate constant.

Table 1. Transfer coefficients, diffusion coefficients, and standard rate constants of all $\text{Co}_3\text{V}_2\text{O}_8$ electrodes.

| Sample Code | Transfer Coefficient (α) | | Diffusion Coefficient (cm^2/S) $\times 10^{-7}$ | | Standard Rate Constant (k^0) (cm/S) $\times 10^{-5}$ | |
|-------------|-----------------------------------|-----------|---|-----------|--|-----------|
| | Reduction | Oxidation | Reduction | Oxidation | Reduction | Oxidation |
| CVO_U_4h | 0.30 | 0.27 | 1.98 | 2.30 | 7.49 | 6.58 |
| CVO_U_7h | 0.27 | 0.24 | 1.67 | 2.54 | 12.9 | 11.2 |
| CVO_U_10h | 0.25 | 0.22 | 4.26 | 4.51 | 18.6 | 14.2 |
| CVO_U_16h | 0.26 | 0.22 | 3.14 | 3.38 | 18.6 | 10.8 |

Here, A represents the electrode area, C represents the electrolyte concentration, v represents the scan rate, R represents the universal gas constant, T represents the absolute temperature, F represents Faraday's constant, D represents the diffusion constant, α represents the transfer coefficient, n represents the number of moles participating in the chemical reaction, E_p represents the peak potential, and E^0 represents the formal potential. The transfer rate constant (k^0) was explored to analyze electrochemical kinetics and establish the nature of the reaction process, whether reversible, irreversible, or quasi-reversible. As illustrated in Figure 8c,d, the k^0 values were determined using the cyclic voltammetry (CV) profile using the peak current and corresponding potential. Depending on the value of k^0 , it may be feasible to identify whether the reaction is irreversible, reversible, or quasi-reversible. $k^0 > 10^{-1}$ for reversible chemical processes and $k^0 < 10^{-5}$ for irreversible chemical reactions. Chemical reactions with $10^{-1} < k^0 < 10^{-5}$ are categorized as quasi-reversible. All electrodes have k^0 values ranging between 10^{-1} and 10^{-5} , implying that the charging

and discharging processes are quasi-reversible. The transfer coefficient α is computed and listed in Table 1, and outcomes vary between 0.22 and 0.30, implying that the reaction is quasi-reversible. The areal capacitance, areal energy density, and areal power density of all CVO_U electrodes were calculated from the GCD profile and Equations (10)–(12). Figure S5 shows the GCD profiles of all the electrodes. The charging and discharging times of all electrodes were altered in accordance with the surface microstructural changes induced by the hydrothermal reaction time. The surface microstructure of the nanowires exhibited a shorter discharging time when compared to the other electrode, as shown in Figure 6b. The nanowire microstructure demonstrated a progressive expansion as the hydrothermal reaction time reached 7 hours, resulting in extended charging and discharging durations, potentially attributed to the development of a wire network through lateral joining. When the hydrothermal reaction time is increased to 10 h, the nanowires begin to form bundles, and empty spaces arise between the bundles. The void spaces between the bundles are beneficial for charging and discharging the ions, and their effects were observed in the GCD profile shown in Figure 6a. The CVO_U_10h electrode showing the longer charging and discharging times demonstrated excellent areal energy density and power density. For the hydrothermal reaction time of 16 h, the thickness of the nanowires increased and the void spacing between the bundles decreased, decreasing the charging and discharging times. Overall, the electrode prepared with a 10 h hydrothermal reaction shows excellent charging and discharging times, possibly due to the uniform nanowire microstructure with bundle arrangement and void spaces between the bundles. The areal capacitance, areal energy density, and power density of the electrode were calculated using Equations (10)–(12) [55,56]. The CVO_U_10h electrode shows an areal capacitance of 4.67 F/cm^2 at a current density of 3 mA/cm^2 , with an energy density of $94 \mu\text{Wh/cm}^2$ and a power density of $573 \mu\text{W/cm}^2$. The rest of the electrodes areal capacitances, energy densities, and power densities are listed in Table 2. In an electrochemical cell, electrochemical impedance spectroscopy was employed for assessing solution resistance (R_s) and charge transfer resistance (R_{ct}). R_s is the solution resistance originating primarily from ion transfer resistance through an interface between the electrolyte and electrode material, estimated using a Nyquist plot at the low-frequency intercept on the x -axis. R_{ct} is the charge transfer resistance measured from the semicircle diameter in the EIS spectra. Figure 6c,d illustrates the EIS spectra of all CVO-U electrodes in the frequency range of 10^5 to 10^{-1} Hz . In the EIS investigation, the impact of hydrothermal reaction time on surface morphological tailoring was observed. At first, nanowires were observed in FESEM, and the electrode exhibited an R_s of 3.01Ω and an R_{ct} of 3.91Ω , which might be attributable to the nanowire microstructure of the CVO_U_4h electrode. Once the reaction period extended to 7 h, the surface microstructure was tailored to establishing nanowires that were connected laterally to each other, and some nanowires formed looping structures, resulting in a network-like microstructure. The series resistance of the electrode fell to 2.09Ω owing to lateral linking; however, R_{ct} rose, probably due to the connection of the nanowire tips in the CVO_U_7h electrode. This impact was found in the GCD analysis, particularly the capacitance study. Following a 10-h hydrothermal reaction duration, nanowires continued to form bundles with the highest lateral linking and void spacing between bundles, and all wire tips were free. The series resistance (R_s) and charge transfer resistance (R_{ct}) of the CVO_U_10h electrode decreased to 2.01Ω and 2.24Ω , respectively, due to substantial lateral linking and free ends of the nanowires, and this impact was noticed in the GCD profile due to an increase in charging and discharging times. The tiny values of R_s and R_{ct} may improve the electrode's charging and discharging time. As the hydrothermal reaction time rose to 16 h, dense bundles with increasing nanowire thickness were identified, affecting ion diffusion, as well as R_s and R_{ct} values, and originating in a drop in specific capacitance in the GCD profile.

The CVO_U_10h electrode possessed the lowest R_s and R_{ct} values compared to the other electrodes, which might be due to laterally connected nanowires producing nano bundles with void spacing and demonstrating good supercapacitor performance. The values of R_s and R_{ct} are listed in Table 2.

$$\text{Areal Capacitance } (C_a) = \frac{T_d \times I_d}{dV \times A} \quad (10)$$

$$\text{Areal Energy Density } (ED_a) = \frac{C_a \times dV^2}{7200} \quad (11)$$

$$\text{Areal Power Density } (PD_a) = \frac{ED_a \times 3600}{T_d} \quad (12)$$

Table 2. Areal capacitance, energy density, power density, series resistance, and charge transfer resistance of $\text{Co}_3\text{V}_2\text{O}_8$ electrodes.

| Sample Code | Areal Capacitance (C_a) F/cm ² | Areal Energy Density (ED_a) $\mu\text{Wh}/\text{cm}^2$ | Areal Power Density (PD_a) $\mu\text{W}/\text{cm}^2$ | R_s (Ω) | R_{ct} (Ω) |
|-------------|---|--|--|--------------------|-----------------------|
| CVO_U_4h | 2.86 | 56 | 567 | 3.01 | 3.91 |
| CVO_U_7h | 3.82 | 77 | 570 | 2.07 | 8.98 |
| CVO_U_10h | 4.67 | 94 | 573 | 2.02 | 2.21 |
| CVO_U_16h | 2.76 | 56 | 570 | 11.8 | 53 |

Here, C_a is the areal capacitance, T_d is the discharging time, I_d is the current density, dV is the potential window of the GCD profile, A is the area of the electrode, ED_a is the area energy density, and PD_a is the areal power density. The EIS spectra employed frequency-dependent real and imaginary impedance [22]. The following algorithms were employed to determine real and imaginary capacitance values:

$$C' = \frac{Z''(\omega)}{\omega |Z(\omega)|^2} \quad (13)$$

$$C'' = \frac{Z'(\omega)}{\omega |Z(\omega)|^2} \quad (14)$$

Here, $Z(\omega)$ denotes complex impedance, $Z'(\omega)$ is the real part of complex impedance, and $Z''(\omega)$ is the imaginary part of complex impedance and represents the ' f ' frequency. Figure S6 illustrates C' and C'' , which represent real and imaginary capacitance. The impact of the surface microstructure on C' and C'' was observed. The electrode CVO_U_10h exhibited the highest values for both C and C'' compared to other electrodes. This might be attributed to laterally linked nanowires with void spacing between nanowire bundles.

3.3. Electrochemical Properties of the CVO_U_10h//AC ASC Device

To examine the actual application of the designed CVO_U_10h electrode, an asymmetric supercapacitor with two electrodes, one coated with CVO_U_10h and a second with activated carbon, was fabricated. The electrode method of preparation was exactly the same for both electrodes, with the exception of the CVO_U_10h electrode, which used $\text{Co}_3\text{V}_2\text{O}_8$ nanoparticles as the active material, while the other electrode used activated carbon. The electrode arrangement was encased in paraffin paper, and the electrolyte was 2M KOH. The two electrodes were coated in paraffin paper and separated by filter paper. Figure 9g depicts a schematic of the two electrodes. Cyclic voltammetry (CV), the galvanostatic charge–discharge (GCD), and electrochemical impedance spectroscopy (EIS)

were employed to look into the chemical characteristics of asymmetric supercapacitor (ASC) electrodes. The potential window of the ASC was maintained at 1.6V using the CV profile of CVO_U_10 and AC from Figure S7a. The plots for the CV, GCD, and EIS of AC are presented in Figure S7b, S7c, and S7d, respectively. Figure 9a depicts the CV profile of the ASC at various potentials ranging from 0.8 to 1.6 V. The potential window was raised to 1.6 V without significant polarization, and this potential was retained for future use. Figure 9b also shows the CV profile of the CVO_U_10h//AC at various scan rates (20–100 mV/s). GCD profiles of the CVO_U_10h//AC ASC at various potentials are displayed in Figure 9d,c, including 8 mA/cm² current density and various current densities with a constant potential of 1.6V. The areal capacitance (C_a), areal energy density (ED_a), and power density (PD_a) of the CVO_U_10h//AC ASC were calculated using GCD profiles at various current densities. Using Equations (10)–(12), the volumetric capacitance (C_v) was calculated to be 1.43 F/cm³, and the volumetric energy density (ED_v) was found to be 511 µWh/cm³ at a 40 mW/cm³ volumetric power density (PD_v) and an areal capacitance of 230 mF/cm², with an areal energy density and power density 81 µWh/cm³ at 6.4 mW/cm³ of at an 8 mA/cm² current density. To calculate the volumetric capacitance, the volume of the CVO-U-10h//AC ASC was used instead of the area of the electrode. The obtained results are compared with the reported study in Table 3. Figure 9e depicts the electrochemical impedance spectroscopy of the CVO_U_10h//AC ASC before and after 15 K GCD cycles of stability testing. The CVO_U_10h//AC ASC's R_s value was 7.09 Ω before stability and grew to 11.03 Ω after stability. Figure 9f shows cyclic stability over 15 K cycles. The capacity retention of the CVO_U_10h//AC ASC electrode was reported to be 83.40% following stabilization. Overall, the CVO_U_10h//AC ASC electrode, constructed from Co₃V₂O₈ nanoparticles in a 10-h hydrothermal process, demonstrates good electrochemical performance in a three-electrode configuration. The ASC proves to be an efficient electrode material for supercapacitor applications. The practical performance of the CVO_U_10h electrode with two electrode configurations with multiple LEDs or a single LED glowing, respectively, is shown in Figure 9h,i.

Table 3. Comparison of CVO-U-10h//AC ACS with previous studies.

| Sr. No. | Electrode Material | Areal Capacitance | Areal Energy Density | Areal Power Density | Reference |
|---------|---|--------------------------|---------------------------|--------------------------|--------------|
| 1. | CVO-U-10h//AC | 230 mF/cm ² | 81 µWh/cm ² | 6.4 µW/cm ² | Present work |
| 2. | NiO@N-C/CC//Fe ₂ O ₃ @N-C/CC | 127.1 mF/cm ² | 32 µWh/cm ² | 0.8 µW/cm ² | [57] |
| 3. | MoS ₂ -graphene bilayer/textile | 63.73 mF/cm ² | 35.40 µWh/cm ² | 8.4 µW/cm ² | [58] |
| 4. | BiMn _x O _y PVA-KOH Bi ₂ MoO ₆ | 52 mF/cm ² | 18.5 µWh/cm ² | 978.7 µW/cm ² | [59] |
| 5. | V ₂ O ₅ /C | 34.68 mF/cm ² | 1.73 µWh/cm ² | 0.072 µW/cm ² | [60] |
| 6. | NP/MnO ₂ 700//AC | 32.8 mF/cm ² | 18.2 µWh/cm ² | 65.6 µW/cm ² | [61] |
| 7. | V ₂ O ₅ @PEDOT/graphene | 22.4 mF/cm ² | 0.18 µWh/cm ² | 11.0 µW/cm ² | [62] |

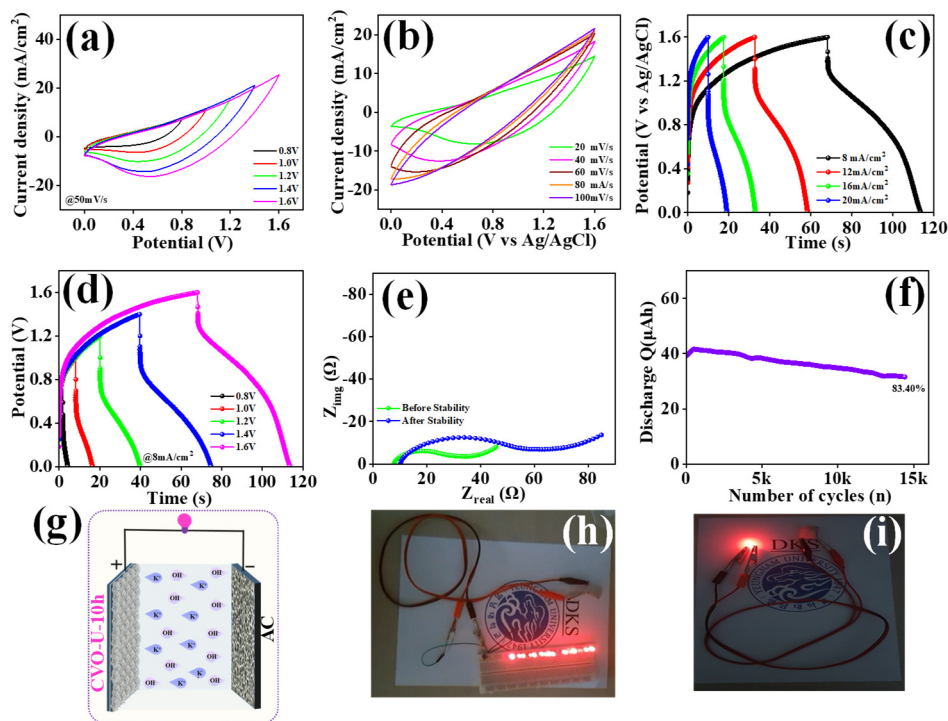


Figure 9. (a) CV profile at different potential windows with a constant scan rate, (b) CV profile at different scan rates with a constant potential window, (c) GCD profile at different current densities with a fixed potential window, (d) GCD profile at a fixed current density with different potential windows, (e) EIS spectra before and after stability over 15 K cycles, (f) cyclic stability for 15 K GCD cycles, (g) schematic representation of the ASC using CVO_U_10h and AC, (h,i) red LED glowing using the ASC of CVO_U_10h // AC.

3.4. Electrocatalysis Study of the CVO_U_10h Electrode

Figure 10a,b presents the linear sweep voltammetry (LSV) plot of the HER study as well as the LSV plot of the OER study, in addition to investigating the electrocatalytic properties of the CVO_U_10h electrode used to investigate the hydrogen evolution reaction (HER) and the oxygen evolution reaction (OER) in a 1M KOH electrolyte. The CVO_U_10h electrode exhibits an overpotential of 259 mV at a current density of 10 mA/cm^2 for HER and 578 mV at 30 mA/cm^2 for OER. The nanowire morphology with vacuum spaces, allowing for a larger number of active sites, might be responsible for the smaller overpotential. Tafel plots were generated employing the LSV profile in order to investigate the reaction kinetics of the CVO_U_10h electrode. Figure 10c,d shows the Tafel plots for HER and OER, respectively. The Tafel slope of the CVO_U_10h electrode for HER is 176 mV/dec, and it is 389 mV/dec for OER. The comparative study of the electrocatalytic performance of $\text{Co}_3\text{V}_2\text{O}_8$ nanoparticles is summarized in Table 4. Figure 10e,f shows the electrochemical impedance spectroscopy of the CVO_U_10h electrode for HER and OER. For HER and OER, the series resistance of the CVO_U_10h electrode is 3.74Ω and 3.56Ω , respectively, while the charge transfer resistance is 12.2Ω and 1.54Ω , respectively. The nanowire microstructure and lateral connections, which form a network with low resistance, are credited with the lower series resistance. As a result of its nanowire structure, the CVO_U_10h electrode has an outstanding overpotential and an acceptable Tafel slope. Figure S8a depicts total water splitting utilizing the CVO_U_10h electrode as both a cathode and anode for hydrogen and oxygen evolution. According to the LSV plot, the total potential required for an overall current density of 10 mA/cm^2 is 1.79 V, rising to 1.82 V after 8 h of stability. The long-term durability of the CVO_U_10h electrode was investigated using chronopotentiometry for 8 h at a current density of 10 mA/cm^2 , as

shown in Figure S8b. Overall, findings illustrate that CVO nanoparticles developed in a 10-h hydrothermal reaction function well as supercapacitors in both three-electrode and two-electrode configurations. Furthermore, the CVO_U_10h electrode exhibits excellent electrocatalytic activity, confirming CVO nanoparticles produced via a 10-h hydrothermal process are a suitable material for supercapacitor and electrocatalytic applications.

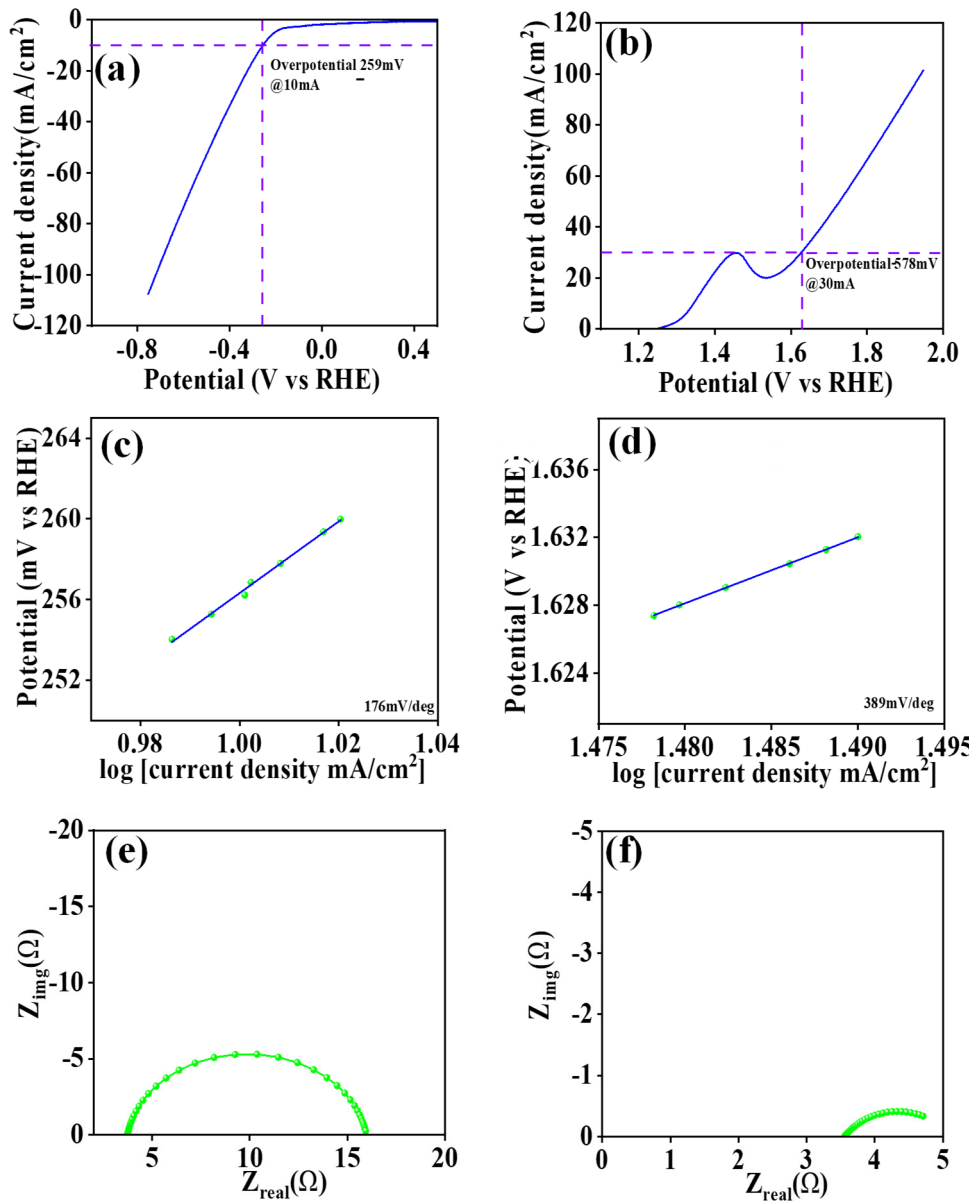


Figure 10. (a,b) LSV plot, (c,d) Tafel plot, (e,f) EIS spectra of OER and HER for the CVO_U_10h electrode.

Table 4. HER and OER Comparative study of CVO-U-10h electrode.

| Electrode | Overpotential mV (HER) | Tafel mV/dec (HER) | Overpotential mV (OER) | Tafel mV/dec (OER) | Reference |
|---|------------------------------|--------------------------|---------------------------------|--------------------------|--------------|
| Co ₃ V ₂ O ₈ | - | - | 190 | 85 | [63] |
| CoO-V ₂ O ₅ | 297 | 159 | 429 | 175 | [64] |
| V _{8.3} -Co-MOF | 293 | 156 | 435 | 78 | [65] |
| Co ₃ V ₂ O ₈ | 278 | 180 | 318 | 130 | [64] |
| Co ₃ V ₂ O ₈ | - | - | 359 | 65 | [66] |
| V _{16.7} -Co-MOF | 271 | 146 | 413 | 77 | [65] |
| CVO_U_10h | 259 | 176 | 578 (30 mA/cm ²) | 389 | Present work |

4. Conclusions

In conclusion, using the hydrothermal approach, nanowires of $\text{Co}_3\text{V}_2\text{O}_8$ nanoparticles were prepared. At 10-h hydrothermal reaction time, the laterally linked nanowires form clusters of nanowire bundles with void spaces between them. The prepared nanowire bundles with void spacing have a considerable areal capacitance of 4.67 F/cm^2 , with energy density and power density of $94 \mu\text{Wh/cm}^2$ and $573 \mu\text{W/cm}^2$, respectively, at 3 mA/cm^2 current density. Activated carbon (AC) and $\text{Co}_3\text{V}_2\text{O}_8$ nanoparticles prepared with a 10-h hydrothermal reaction time were employed to make an asymmetric supercapacitor (ASC). The device has a volumetric capacitance of 1.43 F/cm^3 and an areal capacitance of 781 mF/cm^2 in its two-electrode assembly. The ASC has an areal energy density of $81 \mu\text{Wh/cm}^2$ and an areal power density of 6.4 mW/cm^2 , as well as a volumetric energy density of $511 \mu\text{Wh/cm}^3$ and a volumetric power density of 40 mW/cm^3 at 8 mA/cm^2 current density. Furthermore, electrocatalysis examinations show that electrocatalysis performs effectively in the hydrogen evolution process (HER), the oxygen evolution reaction (OER), and total water splitting. HER electrocatalysis reveals a 259 mV overpotential at a current density of 10 mA/cm^2 , with a Tafel slope of 176 mV/dec. For OER, there is a 578 mV overpotential with a Tafel slope of 389 mV/dec at a current density of 30 mA/cm^2 . The $\text{Co}_3\text{V}_2\text{O}_8$ electrode prepared with a 10-h hydrothermal reaction time acquires 1.78 V for overall water splitting, which rises marginally to 1.8 V after an 8-h stability period. This work demonstrates that nanowire bundles with void spaces prepared with a 10-h reaction time are an acceptable electrode material for energy storage in supercapacitors, as well as HER and OER electrocatalysis applications.

Supplementary Materials: The following supporting information can be downloaded at: <https://www.mdpi.com/article/10.3390/batteries11040118/s1>, Figure S1: FESEM micrographs of (a1–a4) CVO_U_4h, (b1–b4) CVO_U_7h, (c1–c4) CVO_U_10h, and (d1–d4) CVO_U_16h nanowires at different magnifications; Figure S2: EDS spectra of (a) CVO_U_4h, (b) CVO_U_7h, (c) CVO_U_10h, and (d) CVO_U_16h nanowires; Figure S3: BET nitrogen adsorption isotherm plot of CVO_U_10h nanowires; Figure S4: CV profiles of (a) CVO_U_4h, (b) CVO_U_7h, (c) CVO_U_10h, and (d) CVO_U_16h nanowires; Figure S5: (a) GCD profiles of (a) CVO_U_4h, (b) CVO_U_7h, (c) CVO_U_10h, and (d) CVO_U_16h nanowires; Figure S6: Real and imaginary capacitance of (a) CVO_U_4h, (b) CVO_U_7h, (c) CVO_U_10h, and (d) CVO_U_16h electrodes; Figure S7: (a) CV profile of the CVO_U_10h and activated carbon, (b) CV profile at different scan rates, (c) GCD profile at current density, and (d) EIS spectra of activated carbon; Figure S8: (a) LSV plot before and after stability, (b) stability test at 10 mA/cm^2 current density.

Author Contributions: Conceptualization, M.A.Y.; Supervision, D.K.S. All authors have read and agreed to the published version of the manuscript.

Funding: This work was supported by the Technology Innovation Program (#20010170), funded by the Ministry of Trade, Industry & Energy (MOTIE, Korea).

Data Availability Statement: The raw data supporting the conclusions of this article will be made available by the authors on request.

Conflicts of Interest: The authors declare no conflict of interest.

References

1. Lu, Z.; Hu, Z.; Xiao, L.; Xie, Y.; Li, N.; Xi, L.; Chen, W.; Xiao, J.; Zhu, Y. Battery-type Ni-Co-Se hollow microspheres cathode materials enabled by bifunctional N-doped carbon quantum dots with ultrafast electrochemical kinetics for hybrid supercapacitors. *Chem. Eng. J.* **2022**, *450*, 138347. [[CrossRef](#)]
2. Wan, L.; Wang, Y.; Jiang, D.; Zhang, Y.; Xie, M.; Chen, J.; Du, C. Constructing nickel sulfide @ nickel boride hybrid nanosheet arrays with crystalline/amorphous interfaces for supercapacitors. *J. Colloid Interface Sci.* **2023**, *649*, 815–825. [[CrossRef](#)] [[PubMed](#)]

3. Hu, L.; Li, M.; Wei, X.; Wang, H.; Wu, Y.; Wen, J.; Gu, W.; Zhu, C. Modulating interfacial electronic structure of CoNi LDH nanosheets with $Ti_3C_2T_x$ MXene for enhancing water oxidation catalysis. *Chem. Eng. J.* **2020**, *398*, 125605. [[CrossRef](#)]
4. Wu, H.; Zhang, X.; Xue, J.; Zhang, H.; Yang, L.; Li, S. Engineering active sites on hierarchical ZnNi layered double hydroxide architectures with rich Zn vacancies boosting battery-type supercapacitor performances. *Electrochim. Acta* **2021**, *374*, 137932. [[CrossRef](#)]
5. Lv, X.W.; Tian, W.W.; Yuan, Z.Y. Recent Advances in High-Efficiency Electrocatalytic Water Splitting Systems. *Electrochim. Energy Rev.* **2023**, *6*, 23. [[CrossRef](#)]
6. Liu, S.; Yang, J.; Chen, P.; Wang, M.; He, S.; Wang, L.; Qiu, J. Flexible Electrodes for Aqueous Hybrid Supercapacitors: Recent Advances and Future Prospects. *Electrochim. Energy Rev.* **2024**, *7*, 25. [[CrossRef](#)]
7. Wang, G.; Zhang, L.; Zhang, J. A review of electrode materials for electrochemical supercapacitors. *Chem. Soc. Rev.* **2012**, *41*, 797–828. [[CrossRef](#)]
8. Brousse, T.; Bélanger, D.; Long, J. To Be or Not To Be Pseudocapacitive? *J. Electrochem. Soc.* **2015**, *162*, A5185–A5189. [[CrossRef](#)]
9. Lan, Y.; Zhao, H.; Zong, Y.; Li, X.; Sun, Y.; Feng, J.; Wang, Y.; Zheng, X.; Du, Y. Phosphorization boosts the capacitance of mixed metal nanosheet arrays for high performance supercapacitor electrodes. *Nanoscale* **2018**, *10*, 11775–11781. [[CrossRef](#)]
10. Teli, A.M.; Bhat, T.S.; Beknalkar, S.A.; Mane, S.M.; Chaudhary, L.S.; Patil, D.S.; Pawar, S.A.; Efstatiadis, H.; Cheol Shin, J. Bismuth manganese oxide based electrodes for asymmetric coin cell supercapacitor. *Chem. Eng. J.* **2022**, *430*, 133138. [[CrossRef](#)]
11. Thirumal, V.; Yuvakkumar, R.; Senthil Kumar, P.; Ravi, G.; Velauthapillai, D. Direct growth of multilayered graphene nanofibers by chemical vapour deposition and their binder-free electrodes for symmetric supercapacitor devices. *Prog. Org. Coat.* **2021**, *161*, 106511. [[CrossRef](#)]
12. Rawat, P.; Kumar Sharma, P.; Malik, V.; Umapathi, R.; Kaushik, N.; Rhyee, J.S. Emergence of high-performing and ultra-fast 2D-graphene nano-biosensing system. *Mater. Lett.* **2022**, *308*, 131241. [[CrossRef](#)]
13. Tan, Y.B.; Lee, J.M. Graphene for supercapacitor applications. *J. Mater. Chem. A* **2013**, *1*, 14814–14843. [[CrossRef](#)]
14. Mao, B.S.; Wen, Z.; Bo, Z.; Chang, J.; Huang, X.; Chen, J. Hierarchical nanohybrids with porous CNT-networks decorated crumpled graphene balls for supercapacitors. *ACS Appl. Mater. Interfaces* **2014**, *6*, 9881–9889. [[CrossRef](#)]
15. Dubal, D.P.; Chodankar, N.R.; Kim, D.H.; Gomez-Romero, P. Towards flexible solid-state supercapacitors for smart and wearable electronics. *Chem. Soc. Rev.* **2018**, *47*, 2065–2129. [[CrossRef](#)]
16. Lin, J.; Xu, Y.; Wang, J.; Zhang, B.; Li, L.; Wang, X.; He, S.; Zhu, J. A pH-Tailored Anodic Deposition of Hydrous RuO₂ for Supercapacitors. *ChemistrySelect* **2019**, *4*, 8122–8128. [[CrossRef](#)]
17. Snook, G.A.; Kao, P.; Best, A.S. Conducting-polymer-based supercapacitor devices and electrodes. *J. Power Sources* **2011**, *196*, 1–12. [[CrossRef](#)]
18. Sethi, M.; Bhat, D.K. Facile solvothermal synthesis and high supercapacitor performance of NiCo₂O₄ nanorods. *J. Alloys Compd.* **2019**, *781*, 1013–1020. [[CrossRef](#)]
19. Yewale, M.A.; Kadam, R.A.; Kaushik, N.K.; Vattikuti, S.V.P.; Lingamdinne, L.P.; Koduru, J.R.; Shin, D.K. Hydrothermally synthesized microrods and microballs of NiCo₂O₄ for supercapacitor application. *Ceram. Int.* **2022**, *48*, 22037–22046. [[CrossRef](#)]
20. Deokate, R.J.; Kalubarme, R.S.; Park, C.J.; Lokhande, C.D. Simple Synthesis of NiCo₂O₄ thin films using Spray Pyrolysis for electrochemical supercapacitor application: A Novel approach. *Electrochim. Acta* **2017**, *224*, 378–385. [[CrossRef](#)]
21. Rajasekhara Reddy, G.; Ramesh Reddy, N.; Dillip, G.R.; Joo, S.W. In Situ Construction of Binder-Free Stable Battery-Type Copper Cobaltite and Copper Oxide Composite Electrodes for All-Solid-State Asymmetric Supercapacitors: Cation Concentration and Morphology-Dependent Electrochemical Performance. *Energy Fuels* **2022**, *36*, 5965–5978. [[CrossRef](#)]
22. Yewale, M.A.; Kadam, R.A.; Nakate, U.T.; Teli, A.M.; Kumar, V.; Beknalkar, S.A.; Jadhavar, A.A.; Kadam, S.L.; Shelke, N.T.; Shin, D.K. Sphere-shaped CuCo₂O₄ nanostructures battery type electrode for supercapacitor via hydrothermal synthesis approach. *Colloids Surf. A Physicochem. Eng. Asp.* **2023**, *679*, 132541. [[CrossRef](#)]
23. Alqahtani, D.M.; Zequine, C.; Ranaweera, C.K.; Siam, K.; Kahol, P.K.; Poudel, T.P.; Mishra, S.R.; Gupta, R.K. Effect of metal ion substitution on electrochemical properties of cobalt oxide. *J. Alloys Compd.* **2019**, *771*, 951–959. [[CrossRef](#)]
24. Yewale, M.A.; Jadhvar, A.A.; Kharade, R.B.; Kadam, R.A.; Kumar, V.; Nakate, U.T.; Shelke, P.B.; Bobade, D.H.; Teli, A.M.; Dhas, S.D.; et al. Hydrothermally synthesized Ni₃V₂O₈ nanoparticles with horny surfaces for HER and supercapacitor application. *Mater. Lett.* **2023**, *338*, 134033. [[CrossRef](#)]
25. Low, W.H.; Khiew, P.S.; Lim, S.S.; Siong, C.W.; Ezeigwe, E.R. Facile solvothermal designing of graphene/Ni₃V₂O₈ nanocomposite as electrode for high performance symmetric supercapacitor. *J. Alloys Compd.* **2018**, *768*, 995–1005. [[CrossRef](#)]
26. Liu, M.C.; Kong, L.B.; Kang, L.; Li, X.; Walsh, F.C.; Xing, M.; Lu, C.; Ma, X.J.; Luo, Y.C. Synthesis and characterization of M₃V₂O₈ (M = Ni or Co) based nanostructures: A new family of high performance pseudocapacitive materials. *J. Mater. Chem. A* **2014**, *2*, 4919–4926. [[CrossRef](#)]
27. Kadam, R.A.; Yewale, M.A.; Teli, A.M.; Annu; Nakate, U.T.; Kumar, V.; Kadam, S.L.; Shin, D.K. Bimetallic Co₃V₂O₈ microstructure: A versatile bifunctional electrode for supercapacitor and electrocatalysis applications. *Surf. Interfaces* **2023**, *41*, 103267. [[CrossRef](#)]

28. Luo, Z.; Liu, L.; Yang, X.; Luo, X.; Bi, P.; Fu, Z.; Pang, A.; Li, W.; Yi, Y. Revealing the Charge Storage Mechanism of Nickel Oxide Electrochromic Supercapacitors. *ACS Appl. Mater. Interfaces* **2020**, *12*, 39098–39107. [[CrossRef](#)]
29. Jadhav, A.L.; Jadhav, S.L.; Mandlekar, B.K.; Kadam, A.V. Effects of various molarities of nickel oxide on the aggregate 1D–3D structure and its electrochemical activity. *J. Alloys Compd.* **2022**, *925*, 166716. [[CrossRef](#)]
30. Dam, D.T.; Lee, J.M. Three-dimensional cobalt oxide microstructures with brush-like morphology via surfactant-dependent assembly. *ACS Appl. Mater. Interfaces* **2014**, *6*, 20729–20737. [[CrossRef](#)]
31. Ji, Y.; Fang, D.; Wang, C.; Zhou, Z.; Luo, Z.; Huang, J.; Yi, J. Cobalt-doped V₂O₅ nanowire arrays on Ti foil for enhanced lithium-ion storage. *J. Alloys Compd.* **2018**, *742*, 567–576. [[CrossRef](#)]
32. Cao, Y.; Yan, L.; Gang, H.; Wu, B.; Wei, D.; Wang, H. Large gap cobalt-vanadium oxide structure encapsulated in porous carbon for high performance capacitive deionization. *Sep. Purif. Technol.* **2023**, *306*, 122709. [[CrossRef](#)]
33. Saasa, V.; Malwela, T.; Lemmer, Y.; Beukes, M.; Mwakikunga, B. The hierarchical nanostructured Co-doped WO₃/carbon and their improved acetone sensing performance. *Mater. Sci. Semicond. Process.* **2020**, *117*, 105157. [[CrossRef](#)]
34. Liao, M.; Liu, Y.; Hu, Z.; Yu, Q. Novel morphologic Co₃O₄ of flower-like hierarchical microspheres as electrode material for electrochemical capacitors. *J. Alloys Compd.* **2013**, *562*, 106–110. [[CrossRef](#)]
35. Chen, J.; Wu, X.; Selloni, A. Electronic structure and bonding properties of cobalt oxide in the spinel structure. *Phys. Rev. B—Condens. Matter Mater. Phys.* **2011**, *83*, 245204. [[CrossRef](#)]
36. Gao, Z.; Yun, S.; Yang, C.; Zhang, Y.; Dang, J.; Yang, G.; Yang, T.; Qiao, D.; Wang, K. Niobium- and cobalt-modified dual-source-derived porous carbon with a honeycomb-like stable structure for supercapacitor and hydrogen evolution reaction. *J. Colloid Interface Sci.* **2023**, *639*, 33–48. [[CrossRef](#)]
37. Laursen, A.B.; Kegnæs, S.; Dahl, S.; Chorkendorff, I. Molybdenum sulfides—Efficient and viable materials for electro—and photoelectrocatalytic hydrogen evolution. *Energy Environ. Sci.* **2012**, *5*, 5577–5591. [[CrossRef](#)]
38. Simon, P.; Gogotsi, Y.; Dunn, B. Where do batteries end and supercapacitors begin? *Science* **2014**, *343*, 1210–1211. [[CrossRef](#)]
39. Liu, C.; Li, F.; Lai-Peng, M.; Cheng, H.M. Advanced materials for energy storage. *Adv. Mater.* **2010**, *22*, 28–62. [[CrossRef](#)]
40. Vrubel, H.; Moehl, T.; Grätzel, M.; Hu, X. Revealing and accelerating slow electron transport in amorphous molybdenum sulphide particles for hydrogen evolution reaction. *Chem. Commun.* **2013**, *49*, 8985–8987. [[CrossRef](#)]
41. Wang, H.; Zhang, H.; Zhang, D.; Chen, J.; Zhang, S.; Zhang, S.; Yu, J.; Wu, Q.; Li, Q. Toward Enhanced Electrochemical Performance by Investigation of the Electrochemical Reconstruction Mechanism in Co₂V₂O₇ Hexagonal Nanosheets for Hybrid Supercapacitors. *ACS Appl. Mater. Interfaces* **2022**, *14*, 8106–8114. [[CrossRef](#)] [[PubMed](#)]
42. Sun, H.; Chen, X.; Chai, H.; Wang, Y.; Jia, D.; Cao, Y.; Liu, A. 3D porous hydrated cobalt pyrovanadate microflowers with excellent cycling stability as cathode materials for asymmetric supercapacitor. *Appl. Surf. Sci.* **2019**, *469*, 118–124. [[CrossRef](#)]
43. Sharma, G.P.; Gupta, P.K.; Sharma, S.K.; Pala, R.G.S.; Sivakumar, S. Chalcogenide Dopant-Induced Lattice Expansion in Cobalt Vanadium Oxide Nanosheets for Enhanced Supercapacitor Performance. *ACS Appl. Energy Mater.* **2021**, *4*, 4758–4771. [[CrossRef](#)]
44. Thorat, G.M.; Jadhav, H.S.; Roy, A.; Chung, W.J.; Seo, J.G. Dual Role of Deep Eutectic Solvent as a Solvent and Template for the Synthesis of Octahedral Cobalt Vanadate for an Oxygen Evolution Reaction. *ACS Sustain. Chem. Eng.* **2018**, *6*, 16255–16266. [[CrossRef](#)]
45. Singh, D.K.; Yadav, M.; Ganesan, V.; Bhobe, P.A. Cox(VO)yOzNanocrystal-Integrated Covalent Organic Polymers as a Highly Active and Durable Catalyst for Electrochemical Water Oxidation: An Untold Role of the VO²⁺/VO²⁺ Redox Couple. *ACS Appl. Energy Mater.* **2022**, *5*, 2805–2816. [[CrossRef](#)]
46. Han, J.; Liu, X.; Wan, H.; Wu, D.; Chen, G.; Li, J.; Cao, Y.; Ma, R. Composition Tuning of Ultrafine Cobalt-Based Spinel Nanoparticles for Efficient Oxygen Evolution. *ACS Sustain. Chem. Eng.* **2020**, *8*, 5534–5543. [[CrossRef](#)]
47. Fahimi, Z.; Moradlou, O. High-performance solid-state asymmetric supercapacitor based on Co₃V₂O₈/carbon nanotube nanocomposite and gel polymer electrolyte. *J. Energy Storage* **2022**, *50*, 104697. [[CrossRef](#)]
48. Mushtaq, M.W.; Imran, M.; Bashir, S.; Kanwal, F.; Mitu, L. Synthesis, structural and biological studies of cobalt ferrite nanoparticles. *Bulg. Chem. Commun.* **2016**, *48*, 565–570.
49. Samuel, V.; Navale, S.C.; Jadhav, A.D.; Gaikwad, A.B.; Ravi, V. Synthesis of ultrafine BiMnO₃ particles at 100 °C. *Mater. Lett.* **2007**, *61*, 1050–1051. [[CrossRef](#)]
50. Zhang, Q.; Pei, J.; Chen, G.; Bie, C.; Chen, D.; Jiao, Y.; Rao, J. Co₃V₂O₈ Hexagonal Pyramid with Tunable Inner Structure as High Performance Anode Materials for Lithium Ion Battery. *Electrochim. Acta* **2017**, *238*, 227–236. [[CrossRef](#)]
51. Teng, Y.; Li, Y.; Yu, D.; Meng, Y.; Wu, Y.; Zhao, X.; Liu, X. The Microwave-Assisted Hydrothermal Synthesis of CoV₂O₆ and Co₃V₂O₈ with Morphology Tuning by pH Adjustments for Supercapacitor Applications. *ChemistrySelect* **2019**, *4*, 956–962. [[CrossRef](#)]
52. Zheng, L.; Xiao, Z.; Wang, X.; Xi, Y.; Zhai, S.; Fu, X.; Hao, J.; An, Q.; Yang, D. Biomass-Assisted Construction of Carbon-Supported Fe–Co–Cu Trimetallic Oxides/Sulfides for Supercapacitors with Excellent Performance. *ACS Appl. Energy Mater.* **2023**, *6*, 10862–10873. [[CrossRef](#)]

53. Chu, W.; Shi, Z.; Hou, Y.; Ma, D.; Bai, X.; Gao, Y.; Yang, N. Trifunctional of Phosphorus-Doped NiCo_2O_4 Nanowire Materials for Asymmetric Supercapacitor, Oxygen Evolution Reaction, and Hydrogen Evolution Reaction. *ACS Appl. Mater. Interfaces* **2020**, *12*, 2763–2772. [[CrossRef](#)] [[PubMed](#)]
54. Kulurumotlakatla, D.K.; Raghavendra, K.V.G.; Vinodh, R.; Saeed, G.; Muralee Gopi, C.V.V. Facile hydrothermal synthesis of copper oxide microspheres decorated with nickel sulfide nanoparticles battery-type electrode materials for high-energy-density hybrid supercapacitors. *J. Energy Storage* **2025**, *110*, 115327. [[CrossRef](#)]
55. Patil, A.M.; Moon, S.; Jadhav, A.A.; Hong, J.; Kang, K.; Jun, S.C. Modifying Electronic Structure of Cation-Exchanged Bimetallic Sulfide/Metal Oxide Heterostructure through In Situ Inclusion of Silver (Ag) Nanoparticles for Extrinsic Pseudocapacitor. *Adv. Funct. Mater.* **2023**, *33*, 2305264. [[CrossRef](#)]
56. Patil, A.M.; Wang, J.; Li, S.; Hao, X.; Du, X.; Wang, Z.; Hao, X.; Abudula, A.; Guan, G. Bilateral growth of monoclinic WO_3 and 2D $\text{Ti}_3\text{C}_2\text{T}_x$ on 3D free-standing hollow graphene foam for all-solid-state supercapacitor. *Chem. Eng. J.* **2021**, *421*, 127883. [[CrossRef](#)]
57. Cai, D.; Du, J.; Zhu, C.; Cao, Q.; Huang, L.; Wu, J.; Zhou, D.; Xia, Q.; Chen, T.; Guan, C.; et al. Iron Oxide Nanoneedles Anchored on N-Doped Carbon Nanoarrays as an Electrode for High-Performance Hybrid Supercapacitor. *ACS Appl. Energy Mater.* **2020**, *3*, 12162–12171. [[CrossRef](#)]
58. Islam, M.R.; Afroz, S.; Karim, N. Scalable Production of 2D Material Heterostructure Textiles for High-Performance Wearable Supercapacitors. *ACS Nano* **2023**, *17*, 18481–18493. [[CrossRef](#)]
59. Balamurugan, K.; Velmurugan, R.; Subramanian, B. Effect of in situ annealing on pulsed laser ablated mixed metal oxide ($\text{Bi}_x\text{M}_y\text{O}_z$; M=Mn, Mo) thin film electrodes for flexible hybrid supercapacitor devices. *Mater. Today Chem.* **2024**, *35*, 101908. [[CrossRef](#)]
60. Zhou, H.; Zheng, S.; Guo, X.; Gao, Y.; Li, H.; Pang, H. Ordered porous and uniform electric-field-strength micro-supercapacitors by 3D printing based on liquid-crystal V_2O_5 nanowires compositing carbon nanomaterials. *J. Colloid Interface Sci.* **2022**, *628*, 24–32. [[CrossRef](#)]
61. Mohanty, R.I.; Mukherjee, A.; Bhanja, P.; Jena, B.K. Novel microporous manganese phosphonate-derived metal oxides as prospective cathode materials for superior flexible asymmetric micro-supercapacitor device. *J. Energy Storage* **2023**, *72*, 108730. [[CrossRef](#)]
62. Wang, L.; Shu, T.; Guo, S.; Lu, Y.; Li, M.; Nzabahimana, J.; Hu, X. Fabricating strongly coupled V_2O_5 @PEDOT nanobelts/graphene hybrid films with high areal capacitance and facile transferability for transparent solid-state supercapacitors. *Energy Storage Mater.* **2020**, *27*, 150–158. [[CrossRef](#)]
63. Gyanprakash, D.M.; Gupta, P.K.; Sharma, G.P.; Pala, R.G.S. Surface-enhanced OER activity in $\text{Co}_3\text{V}_2\text{O}_8$ using cyclic charge-discharge to balance electrocatalytic active site generation and degradation. *Electrochim. Acta* **2021**, *367*, 137538. [[CrossRef](#)]
64. Yang, Z.; Chen, H.; Xiang, M.; Yu, C.; Hui, J.; Dong, S. Coral reef structured cobalt-doped vanadate oxometalate nanoparticle for a high-performance electrocatalyst in water splitting. *Int. J. Hydrogen Energy* **2022**, *47*, 31566–31574. [[CrossRef](#)]
65. Fang, W.; Dang, J.; Hu, Y.; Wu, Y.; Xin, S.; Chen, B.; Zhao, H.; Li, Z. Electronic distribution tuning of vanadium-cobalt bimetallic MOFs for highly efficient hydrazine-assisted energy-saving hydrogen production. *Electrochim. Acta* **2023**, *439*, 141682. [[CrossRef](#)]
66. Xing, M.; Kong, L.B.; Liu, M.C.; Liu, L.Y.; Kang, L.; Luo, Y.C. Cobalt vanadate as highly active, stable, noble metal-free oxygen evolution electrocatalyst. *J. Mater. Chem. A* **2014**, *2*, 18435–18443. [[CrossRef](#)]

Disclaimer/Publisher's Note: The statements, opinions and data contained in all publications are solely those of the individual author(s) and contributor(s) and not of MDPI and/or the editor(s). MDPI and/or the editor(s) disclaim responsibility for any injury to people or property resulting from any ideas, methods, instructions or products referred to in the content.